Viscous and Inviscid Strato-Rotational Instability: Supplementary Information

Luke J. M. Robins[1]†, Evy Kersalé[1] and Chris A. Jones[1]‡

[1]Department of Applied Mathematics, University of Leeds, Leeds, LS2 9JT, UK

(Received 23 February 2018; revised 3 October 2019; accepted 13 March 2020)

In this supplementary information (SI) about the onset of SRI we consider in more detail some of the issues raised in the main paper. Figures S1 to S7 illustrate the transition from radiative instability (RI) modes in region ζ (see figure 2 of the main paper) to the inner boundary-trapped SRI in region γ. Figures S8 to S12 give further information about the RI modes. Figures S13 to S15 illustrate the three modes at the triple point, T, shown in figure 2 at $\eta = 0.081617$, $\mu = 0.057637$. Figure S16 shows the mode type found by Leclerq et al. (2016) which can be compared with the viscous critical mode in figure 13(c,d) of the main paper. Figures S17 and S19 show two inviscid-type viscous SRI modes in region γ of figure 2, together with one of their inviscid counterparts (S18), which are not the first modes to onset as Re is increased, but which do show Kelvin wave behaviour as found in some previous studies of SRI. Figure S20 shows the same inviscid-type viscous SRI mode shown in figure 8(a,b) typifying behaviour in region δ of figure 2, and figure S21 is its inviscid counterpart. Figure S22 gives additional information about the formation of closed unstable domains and the point of continuity, discussed in § 6.2 and § 6.3 of the main text.

1. Details of the plots

The plots are of three types, (i), (ii), and (iii), excluding figure S22 which is a regime diagram. Table 1 shows the type of each plot.

1.1. *Type (*i*) plots*

These viscous plots have two parts, the left-hand plot showing a section at $\theta = 0$ of the rz-plane, and the right-hand plot showing a section at $z = 0$ of the $r\theta$-plane. The colour contours of the left-hand plot are of u_θ, the normal velocity of the section, and the arrows show the direction and relative magnitude of the flow in the rz-plane. The colour contours of the right-hand plot are of u_z, the normal velocity of the section, and the arrows show the direction and relative magnitude of the flow in the $r\theta$-plane. All velocities are normalised by the maximum of u_r over the eigenfunction. The colour scheme for the contours is customised to show up any wave-like behaviour, which can have only a relatively small amplitude compared with the flow near the inner cylinder in wide gap cases. To achieve this, the colours change rapidly near zero, which corresponds to white. In the bgr-colour scheme, the 64 colours are defined as

$$r(j) = g(j) = 0.9206\frac{j-1}{31},\ b(j) = 1,\ 1 \leqslant j \leqslant 32, \quad \text{negative values},$$

$$b(j) = g(j) = 0.9206\frac{64-j}{31},\ r(j) = 1,\ 33 \leqslant j \leqslant 64, \quad \text{positive values}.$$

† Email addresses for correspondence: luke.robins@cantab.net
‡ Email addresses for correspondence: pmtcaj@leeds.ac.uk

TABLE 1. Table of the supplementary figure types.

Type (i)	S1	S3	S5	S7	S8	S9	S13	S14	S15	S16	S17	S19	S20
Type (ii)	S2	S4	S6	S18	S21								
Type (iii)	S10	S11	S12										

For the figure 13(c,d) of the main paper, and figure S16(a,b) of the SI, where there is an outer region where the wave amplitude is close to zero, a colour scheme with an odd number of colours (65) is preferred, where this colour scheme has colours 1 to 32 as above, but has $r(33) = g(33) = b(33) = 1$ (white) and

$$b(j) = g(j) = 0.9206\frac{65-j}{31},\ r(j) = 1,\ 34 \leqslant j \leqslant 65.$$

To make the waves even more visible, solid contours are plotted at magnitudes ± 0.005 and ± 0.015, with the positive contours being solid and the negative contours dashed. These contour amplitudes are the same for all the plots. As with the colours, the contours are of u_θ in the left-hand plot and u_z in the right-hand plot.

1.2. *Type (*ii*) plots*

These are derived using the inviscid equations rather than the viscous equations as described in § 2.1 of the main paper. The layout and the colour scheme are the same as in the type (i) plots, with contours again plotted at magnitudes ± 0.005 and ± 0.015 to enable the inviscid plots to be directly compared with the viscous type (i) plots.

1.3. *Type (*iii*) plots*

These are also derived using the inviscid equations. They were created using the MATLAB routine bvp5c, which iterates on the eigenvalue. The initial guess for the eigenvalue was supplied using our Chebyshev code, which is matrix based and does not require an initial guess for the eigenvalue. Because it requires a reasonably accurate initial eigenvalue guess, routine bvp5c is not suitable for exploring parameter space, but it is useful for checking that the results from the Chebyshev based code are accurate, as it is completely independent of the Chebyshev code. The complex radial eigenfunction $u_r(r)$ is derived by solving equation (2.9) of the main paper, and the corresponding complex eigenfunctions for $u_\theta(r)$ and $u_z(r)$ are then calculated. In the type (iii) plots the real parts of the velocity components are shown in red and the imaginary parts in blue, both as functions of radius r. The eigenfunctions are normalized to make the pressure perturbation unity at the inner boundary.

2. Transition from radiative instability (RI) to an inner boundary-trapped SRI

The supplementary figures S1 to S7 (see also S14) show how the RI evolves continuously into an inner boundary-trapped mode, as η and μ move from region ζ to region γ of figure 2. Figure S1 is the same as figure 13(a,b) in the main paper. It is at $\eta = \mu = 0.1$, not far from the triple point T of figure 2, with $m = 1$. The wave-like character is clear, but note that even this close to the triple point, the amplitude of the wave part of the flow is small compared to the amplitude of the flow near the inner boundary. The colour scheme has been designed to emphasise features with an amplitude close to zero. The amplitude near the boundary is around unity but the contours have magnitude ± 0.005 and ± 0.015, fixed for all plots, so the wave amplitude is only a few percent

of the wall amplitude. However, there clearly are radiating waves, and the WKBJ-inviscid theory predicts wave-like behaviour beyond $r = 0.2480$ which is indeed about where the waves start. At $N = Fr = 1$, $|\Phi|$ is less than N, so we don't have $\mathcal{R}[\Phi] = N$ for these parameters. Waves continue to the outer boundary. The local radial wavelength according to the WKBJ-inviscid theory is

$$\lambda = 2\pi/\sqrt{k^2[\Phi^2 - 2Z\Omega)/(N^2 - \Phi^2)}$$

where Φ is the Lagrangian frequency $\omega - \Omega$ ($m = 1$). λ is a decreasing function of r in these plots, so the minimum value is at r_{out}. For the figure S1 parameters, $\lambda(r_{out}) = 0.2226$, which fits quite well with the radial wavelength near $r = 1$ in figure S1, one full wavelength fitting in between about $r = 0.9$ and $r = 1.1111$.

Figure S2 is the inviscid counterpart of figure S1. $\eta = \mu = 0.1$, $m = 1$, $Fr = 1$ as in figure S1. The local maximum of the growth rate over k is at $k = 53.7661$, and the growth rate there is $\sigma = 0.003591$ with frequency $\omega = 0.60302$. These k and ω values are similar, but not identical, to those in the viscous plot above. The wave contours are more rectangular in the inviscid case, suggesting slightly more back-reflection from the outer boundary, and the wave amplitude is slightly larger. These differences are not surprising, as Re in figure S1 is not so large that viscosity is completely unimportant.

Figure S3 has $\eta = \mu = 0.15$ moving towards the figure 7 value (marked in figure 2) in the $\eta\mu$-plane. Comparing with figure S1, we see there is still evidence of waves. The WKBJ-inviscid theory predicts wave-like behaviour beyond $r = 0.4558$ quite a bit further out than figure S1, and again the viscous plots bear this out. But the most important change is that the radial wavelength of the waves has increased so that only about one full wavelength fits into the gap in the radial direction. However, we think it would still be reasonable to call this an example of RI. At $r = 1.1764 = r_{out}$ the local $\lambda = 0.5345$ on WKBJ-inviscid theory, but it increases as r is reduced. A half-wavelength near the outer boundary occupies about a width of 0.27, so WKBJ-inviscid theory is still doing a reasonable job of predicting the wavelength of the waves.

Figure S4 is the inviscid counterpart of figure S3. $\eta = \mu = 0.15$, $m = 1$, $Fr = 1$. The local maximum of growth rate over k is at $k = 28.59$, the growth rate is $\sigma = 0.00175$ and $\omega = 0.5958$. These k, ω values are similar to those of the viscous figure above, see the S3 figure caption.

Figure S5 has $\eta = \mu = 0.20$ moving further towards the figure 7 value in the $\eta\mu$-plane. Comparing with figure S3, we see there isn't much evidence of waves: the wavelength has continued to increase, so there isn't room in the gap for wave-like behaviour. The WKBJ-inviscid theory predicts wave-like behaviour beyond $r = 0.9259$, which is not far from the outer cylinder, but the problem is there is no room to fit in the long wavelength waves any more. WKBJ-inviscid $\lambda = 1.3782$ at r_{out}, clearly too big to see a wavelength, and λ increases as r reduces. During our research we initially thought of this mode as a type of RI, since it is clearly continuously connected to figures S1 and S3, but it has changed its character, so we now prefer to call this an inner boundary-trapped mode in region γ of figure 2 of the main paper. There is no sharp boundary between region ζ and region γ in figure 2, because the transition is gradual, as the wave-like behaviour disappears in a gradual manner.

Figure S6 is the inviscid counterpart of figure S5, again with $\eta = \mu = 0.20$, $m = 1$, $Fr = 1$. The local maximum of growth rate over k is at $k = 23.46$, the growth rate $\sigma = 0.000335$ and $\omega = 0.6656$, somewhat similar k and ω values to the viscous figures above, see the figure S5 caption. However, by contrast with figures S3 and S4, note that the wavenumber k at maximum growth rate is now significantly higher than the viscous preferred k. So this is an example where the inviscid mode has some similarities to the viscous mode but is beginning to diverge from it as μ increases. When we get to $\mu = 0.45$ in the next viscous plot, figure S7, there is no inviscid mode with a k-value close to the viscous critical k so all contact with the inviscid case is lost.

Figure S7 shows a viscous mode with $\eta = 0.4$, $\mu = 0.45$ and is the same as figure 7(a,b). It is pretty similar to figure S5, so all the modes in the γ region with μ greater than 0.2 are probably all going to look like this (consistent with other runs not shown). The point at which the Lagrangian frequency equals the epicyclic frequency has disappeared, as could be predicted from the rapid increase of the critical r at which this occurs as μ is increased. It is notable that here the slope of the contour lines in the rz-plane has disappeared too. This sequence of figures S1 to S7 shows how the RI continuously morphs into the inner boundary-trapped SRI.

Figures S8 and S9 show viscous modes with $\eta = \mu = 0.1$. They have k which are local minima of Re, but are not the global minimum. Figure S1 shows the global minimum at these η, μ, Fr parameter values. Figure S8 has $k = 50.126$, slightly less than the figure S1 value, and there are fewer radial waves fitting in. The local minimum of Re is 114199, much bigger than the figure S1 value. Figure S9 has $k = 54.06$, not that different from the S1 value, and the number of radial waves is similar too. These modes are mentioned in the second paragraph of § 7.2, but there isn't space there to show them. As Re is increased from 12565 at this k value, the growth rate first increases and then decreases, going to zero and so restabilising. As Re is further increased it becomes unstable again at $Re = 145040$ with a very slightly different k value. It is interesting to compare figure S9 and figure S1. In S1 the waves slope in the rz and $r\theta$-planes at a more or less fixed angle, but in S9 there is a sharp change near $z = 0$ and $\theta = 0$. Also, figure S9 resembles the inviscid figure S2 more closely than figure S1 does. The sharp change in eigenfunction shape signals more wave reflection back from the outer boundary (radial wave structure more standing-wave-like), as expected from the much higher Re values 114199 and 145040 and correspondingly less wave attenuation for figures S8 and S9, versus 12565 for figure S1.

3. More inviscid RI runs

Figures S10, S11 and S12 display inviscid eigenfunctions in type (iii) style, see § 1.3. Real parts are in red, imaginary parts in blue. Figure S10 is at the local maximum growth rate (as k is varied) which is closest to the figure S1 value of k. This is the same case as figure S2, plotted in a different way, and was done partly to independently check the numerical results coming from the Chebyshev code. Note that it has the same number of radial wavelengths as the viscous figures S1 and figure S9. Figures S11 and S12 are other local maxima in growth rate over k cases, closest to the figure S10 local maximum. Note figure S11 has one half a radial wavelength less, and figure S12 one half a radial wavelength more. Note also that the fastest growth rate case of the three is not figure S10 but figure S11, which has growth rate 0.00398 compared to the figure S10 growth 0.003591. The fastest growth rate continues to increase as you reduce the number of radial waves in the eigenfunction sequence. So although the viscous mode shown in figure S1 has the lowest critical Reynolds number, the corresponding inviscid mode shown in figures S2 and S10 is not the global fastest growing inviscid mode. Inviscid modes with a smaller number of radial waves fitting inside the domain have a larger local maximum growth rate. Although the inviscid theory clearly has a strong connection with the viscous theory for these RI modes in region ζ of figure 2, the inviscid theory alone would not be a good predictor of which viscous mode is the first to become unstable as Re increases.

4. The three eigenfunctions near the triple point

Figures S13, S14 and S15 show the three very different modes at the triple point T at $\eta = 0.081617$ and $\mu = 0.057637$, which all onset at the same value of $Re = 17493$. S13 is the wide-gap mode, similar to figure 9 in the main paper, S14 is the RI similar to figure 13 in the main paper, and S15 is the inviscid-type mode similar to figure 8 of the main paper. This indicates that

the modes in the triple point region do preserve their shape in different parts of the parameter space, except that the RI morphs into the inner boundary-trapped mode at larger μ, and the inviscid-type δ mode morphs into a β type mode (figures 5 and 6 of the main paper).

5. Connection with Leclerq et al. (2016)

Leclerq et al. (2016) mention that they found radiative instability at $\eta = 0.417$, with $N = 0.5\Omega_{\rm in}$ which is equivalent to their Richardson number $Ri = N^2/\Omega_{in}^2$ being 0.25. They had $m = 1$ and $Re = 10^6$. They don't say exactly what their values of μ and k were for their figure 7a, but the caption suggests μ was just below the Rayleigh curve value which at $\eta = 0.417$ is $\mu = 0.173889$. So here we put $\mu = 0.17$ just below the Rayleigh curve. The critical k for maximum growth rate is then at $k = 123.9$ and then $\sigma = 0.06789 - 0.86135i$. The corresponding figure here is figure S16, which looks very like their figure 7a.

Since $\mu < \eta^2$, Z is negative, so there is no real epicyclic frequency so no point where the Lagrangian frequency equals the epicyclic frequency. So this is a bit different from Le Dizès & Riedinger (2010) who considered regimes which are Rayleigh-stable. However, in figure S16 there is a significant surface at $r = 0.7704$ where $\mathcal{R}[\Phi(r_c)] = 0$ and a surface where $\mathcal{R}[\Phi(r)] = N$ which is at $r = 1.185$, and outside this latter significant surface the amplitude of the disturbance is small. Actually, the r-value at which the amplitude becomes small is nearer $r = 0.95$ rather than $r = 1.185$, see figure S16. The Park & Billant (2013) theory assumes the growth rate is small, and it is here but it is not completely negligible. So the denominator $N^2 - \Phi^2$ doesn't exactly vanish when $\mathcal{R}[\Phi(r_c)] = N$, so the change from wave-like to evanescent takes place over a thin but finite region, and this may explain the slight mismatch of Figure S16 with a wave cut-off at $r = 1.185$.

Note that the Leclerq et al. (2016) example is not a critical viscous mode. At their values of the parameters, there are also modes resembling the simple viscous SRI in our region β that onset at far smaller Re values, just over 100.

6. Connection between Kelvin waves and inviscid-type modes

In figure S17 we show a Kelvin wave mediated viscous SRI, but it is **not** the critical viscous mode at these parameters. The parameters are $\eta = 0.4$, $\mu = 0.45$, $Fr = 1$, $m = 1$, $Re = 71840$, $k = 5.00$, $\omega = 0.598$. Figure 7 in the main paper (figure S7 in this supplementary information) shows the true critical viscous mode, which is of inner boundary-trapped type at these parameters. The mode shown in figure S17 is visible in figure 7(c) of the main paper as the minimum Re of the needle shaped curve near $k = 5$. It is an inviscid-type mode, so it has an inviscid counterpart visible in figure 7(d) of the main paper. It is continuously connected to the inviscid-type mode of figure 8 at $\eta = 0.2$, $\mu = 0.1$ in the main paper, and figure S17 has some resemblance to the eigenfunction shown in figure 8. But the figure 8 SRI has a wide-gap, so the outer boundary Kelvin wave is much weaker than the inner boundary Kelvin wave. In this figure S17 the eigenfunction has waves of comparable amplitudes trapped at both inner and outer boundaries, giving it a Kelvin wave appearance, resembling the Yavneh et al. (2001) Kelvin wave SRI. Figure S18 is the inviscid counterpart of figure S17, also at $\eta = 0.4$, $\mu = 0.45$, $Fr = 1$, $m = 1$. The fastest growing inviscid mode is at $k = 5.024$, very close to the viscous critical k, and here $\sigma = 0.003955$, $\omega = 0.59882$. It is very similar to the viscous figure S17.

We originally expected the Kelvin wave mechanism to be dominant, but it turns out that at $Fr = 1$, the case we concentrated on, there are hardly any Kelvin-wave mediated SRIs at the onset of instability. The closest are the region δ modes, but these are wide-gap whereas the original Yavneh et al. (2001) work focused on narrow gaps. At narrow gaps, SRI fills the whole

gap, see e.g. figure 4 of the main paper in region β of figure 2. These are clearly not Kelvin waves but are inertia-gravity wave mediated SRI.

Of course, at different values of Fr there may well be critical viscous Kelvin-wave SRI, but that is outside the scope of this investigation.

Figures S19 and S20 show how this figure S17 mode morphs into the figure 8 inviscid-type region δ mode. Figure S19 is intermediate between the figure S17 and the figure 8 mode, which is plotted as figure S20 in this type (i) colour scheme. At the figure S19 parameters $\eta = \mu = 0.25$, we are still in region γ of figure 2, so the inner boundary-trapped mode (not shown) onsets first, with Re_c just below 13340. In figure S19 you can see the outer boundary activity fading somewhat as figure 8 (S20) values are approached. At the figure S19 parameter values, there is still activity in the left-hand plot at the outer boundary, but this is considerably reduced in figure S20 at the figure 8 value of $\eta = 0.2$, $\mu = 0.1$. Figure S20 is the same eigenfunction as figure 8, plotted in the alternative type (i) colour scheme. Figure S21 is the inviscid counterpart of figure S20, and hence of figure 8. The fastest growing inviscid mode is at $k = 8.613$ (see figure 8(d) of the main paper), just below the viscous critical $k = 9.067$, and here $\sigma = 0.02789$, $\omega = 0.24978$. Note that because figure S20 has an Re_c of only 670.1, the critical k and ω are slightly changed from the figure S21 values. However, we call this an inviscid-type SRI mode because it is clearly linked to a corresponding inviscid mode.

7. Closed unstable domains and the point of continuity

In section § 6.2 of the main paper we discussed how the closed unstable domains close up as the thin solid curve terminating in the point of continuity X in figure 2 is crossed from right to left. This leads to a discontinuous jump in Re_c across the thin solid curve, which is why we called it the discontinuity curve. In § 6.3 of the main paper, we explained how the closed unstable domains can become engulfed by the inviscid-type modes as shown in figure 12(a) of the main paper. In figure S22, we replot figure 2 of the main paper, but add a new dot-dash curve also terminating in the point X. This dot-dash curve denotes the points in the $\eta\mu$-plane at which the closed unstable domain connects onto the inviscid-type mode.

To understand this behaviour, we concentrate first on figure 6(c) (main paper) on the $m = 1$ curves just above $k = 4$. At Re around 400 we have the closed unstable teardrop, below the needle shaped curve with a minimum Re around 12000. We now move in the $\eta\mu$-plane from $\eta = 0.45$, $\mu = 0.45$, the Fig. 6 cross in figure S22, keeping μ fixed at 0.45 but increasing η (see figure S22). As we do this, the minimum of the needle shaped curve drops down rapidly from $Re = 12000$, while the Re location of the closed unstable domain teardrop increases slightly. At $\eta = 0.5018$, $\mu = 0.45$ the top of the teardrop connects with the bottom of the needle shaped inviscid-type mode. This connection occurs at $Re \approx 2100$, $k \approx 3.92$. To establish this behaviour we monitor the growth rate of the viscous instability maximised over k for a range of Re. If the value of η and μ lie just to the left of the dot-dash curve, as Re is increased the mode becomes unstable as the bottom of the closed unstable domain teardrop is reached. The growth rate first increases with Re, but then starts to diminish. When the top of the teardrop is reached in the kRe-plane, the growth rate goes negative as Re is increased. But on further increasing Re the growth rate goes positive again. On the other hand, if the value of η and μ lie just to the right of the dot-dash curve, the growth rate again increases through zero at the minimum critical Re, and again starts to diminish as Re is further increased. But now it never quite goes negative as Re is increased. So the crucial point is that for η values between the discontinuity curve and the dot-dash curve there is a window of negative growth rate beyond the onset of instability separating the teardrop from the inviscid-type upper branch. Once the dot-dash curve is crossed to the right, this window of negative growth rate disappears, and so does the closed unstable domain.

It is now apparent that there is no jump in critical Re across the dot-dash line, since critical

Re_c occurs at Re well below the window of Re in which negative growth rate is seen. However, the dot-dash curve does denote the right-hand boundary of the closed unstable domain in the $\eta\mu$-plane.

As the point of continuity X is approached, the η window in which closed unstable domains can occur shrinks to zero. The closed unstable domains themselves become very small in the kRe-plane, so the jump in Re as the discontinuity curve is crossed from right to left also becomes small. So X is indeed a point of continuity, because the jump in Re_c as the discontinuity curve is crossed goes to zero as X is approached.

Figure S22(b) is a blowup of the region of figure S22(a) near the point of continuity X at $\eta = 0.2172$, $\mu = 0.1212$. The figure 12(a) point in the $\eta\mu$-plane at $\eta = 0.22$, $\mu = 0.1245$ is shown as a cross, and it can be seen it lies just to the right of the dot-dash line where the window of negative growth rate has just disappeared. The middle of the necked region in figure 12(a), at $k \approx 8.17$ and $Re \approx 636$, is where the growth rate has a saddle point, a minimum as Re varies and a maximum as k varies. If we move gradually leftward in the $\eta\mu$-plane of figure S22(b), at fixed $\mu = 0.1245$, we would first see a tiny closed unstable domain appear when the dot-dash curve is crossed, which would then disappear as the discontinuity curve is crossed.

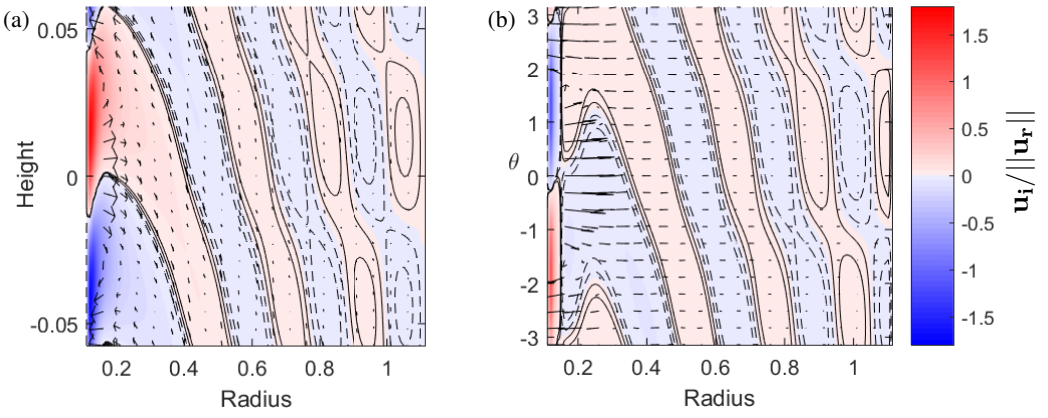

FIGURE S1. Type (i) plots (a), (b) as described in § 1.1. The radiative instability (RI) as the critical viscous mode of instability for stratified Taylor-Couette flow. $\eta = \mu = 0.1$, $m = 1$, $Fr = 1$, and this critical mode onsets at $Re_c = 12565.1$ with $k = 54.72$. $\omega = 0.5888$, $\mathcal{R}[\Phi(r_c)] = 0$ at $r_c = 0.1501$, $\mathcal{R}[\Phi(r_-)] = -\sqrt{2Z\Omega}$ does not occur, but $\mathcal{R}[\Phi(r_+)] = \sqrt{2Z\Omega}$ occurs at $r_+ = 0.2480$, and $\max(|\Phi|) = 0.4888 < N = 1$. This is the same as figures 13(a,b) in the main paper, in region ζ of figure 2, and is replotted to aid comparison with the inviscid plots below.

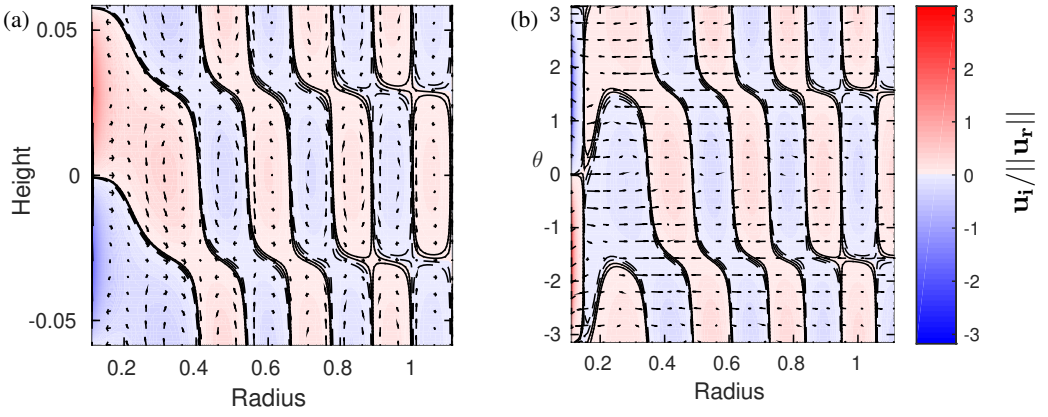

FIGURE S2. Type (ii) plots (a), (b) as described in § 1.2. Inviscid instability at $\eta = \mu = 0.10$, $m = 1$, $Fr = 1$, in region ζ of figure 2. Local maximum of growth rate over k at $k = 53.7661$. Growth rate $\sigma = 0.003591$. Frequency $\omega = 0.60302$. Similar to viscous plot above. Wave contours are more rectangular, and wave amplitude is slightly larger. Frequency ω is close to the figure S1 value, but not quite identical. These differences are not surprising, as Re in figure S1 is not so large that viscosity is completely unimportant. $\mathcal{R}[\Phi(r_c)] = 0$ at $r_c = 0.1480$, $\mathcal{R}[\Phi(r_-)] = -\sqrt{2Z\Omega}$ does not occur, but $\mathcal{R}[\Phi(r_+)] = \sqrt{2Z\Omega}$ occurs at $r_+ = 0.2420$.

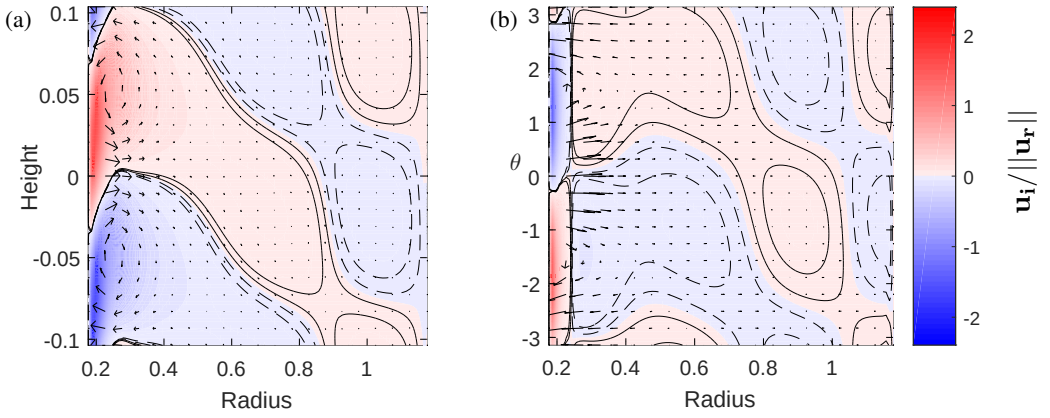

FIGURE S3. Type (i) plots (a), (b) as described in § 1.1. Example of RI as the critical viscous mode of instability for stratified Taylor-Couette flow. $\eta = \mu = 0.15$, $m = 1$, $Fr = 1$, in region ζ in figure 2, and this critical mode onsets at $Re_c = 7193$ with $k = 30.29$. $\omega = 0.5960$, $\mathcal{R}[\Phi(r_c)] = 0$ at $r_c = 0.2412$, $\mathcal{R}[\Phi(r_-)] = -\sqrt{2Z\Omega}$ does not occur, but $\mathcal{R}[\Phi(r_+)] = \sqrt{2Z\Omega}$ occurs at $r_+ = 0.4944$, and $\max(|\Phi|) = 0.446 < N = 1$. Waves still visible, but the radial wavelength has increased compared to figure S1 consistent with WKBJ-inviscid theory.

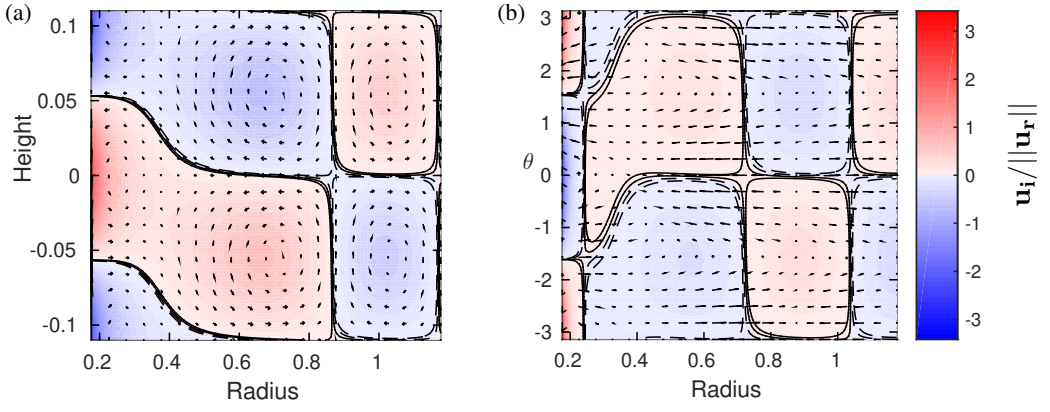

FIGURE S4. Type (ii) plots (a), (b) as described in § 1.2. Inviscid instability at $\eta = \mu = 0.15$, $m = 1$, $Fr = 1$, in region ζ in figure 2. Local maximum of growth rate over k at $k = 28.59$. Growth rate $\sigma = 0.00175$. Frequency $\omega = 0.5958$; k, ω values similar to those of the viscous figure S3 above. $\mathcal{R}[\Phi(r_c)] = 0$ at $r_c = 0.2412$, $\mathcal{R}[\Phi(r_-)] = -\sqrt{2Z\Omega}$ does not occur, but $\mathcal{R}[\Phi(r_+)] = \sqrt{2Z\Omega}$ occurs at $r_+ = 0.4945$.

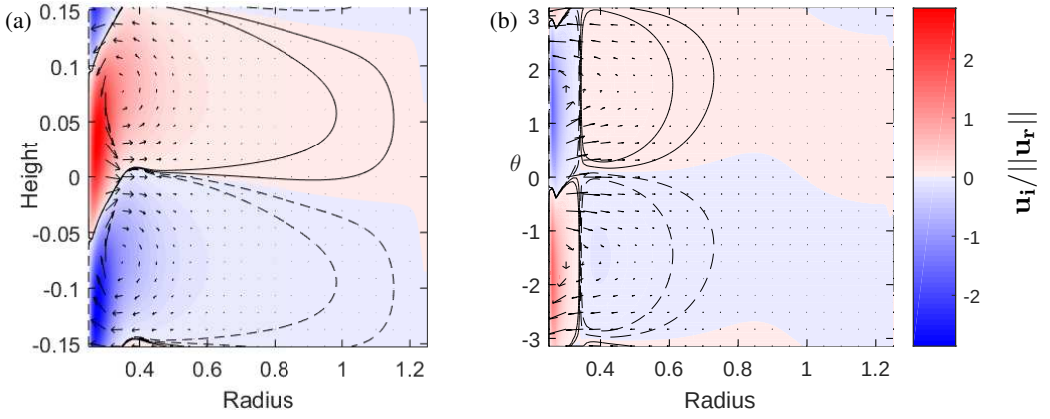

FIGURE S5. Type (i) plots (a), (b) as described in § 1.1. Example of RI as the critical viscous mode of instability for stratified Taylor-Couette flow. $\eta = \mu = 0.20$, $m = 1$, $Fr = 1$, in region γ (but close to region ζ) in figure 2, and this critical mode onsets at $Re_c = 5169$ with $k = 20.62$. $\omega = 0.6168$, $\mathcal{R}[\Phi(r_c)] = 0$ at $r_c = 0.3402$, $\mathcal{R}[\Phi(r_-)] = -\sqrt{2Z\Omega}$ does not occur, but $\mathcal{R}[\Phi(r_+)] = \sqrt{2Z\Omega}$ occurs at $r_+ = 0.9259$, and $\max(|\Phi|) = 0.4168 < N = 1$.
The radiative waves have disappeared. There is a small $\Delta = \Phi^2 - 2Z\Omega > 0$ region (see equation (2.9)), but not big enough to fit in the long radial wavelength waves.

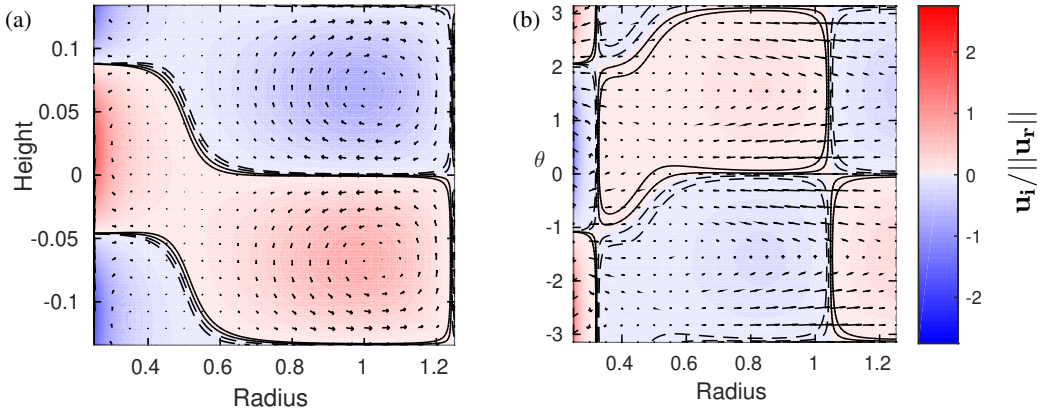

FIGURE S6. Type (ii) plots (a), (b) as described in § 1.2. Inviscid instability at $\eta = \mu = 0.20$, $m = 1$, $Fr = 1$, in region ζ in figure 2. Local maximum of growth rate over k at $k = 23.46$. Growth rate $\sigma = 0.000335$. Frequency $\omega = 0.6656$. Somewhat similar to the viscous figure S5 above. However, note the maximum growth rate k is significantly higher than the viscous preferred k. So this is an example where the inviscid mode has similarities to the viscous mode but is diverging from it as μ increases. When we get to $\mu = 0.45$ in the next viscous plot, all contact with the inviscid mode is lost. $\mathcal{R}[\Phi(r_c)] = 0$ at $r_c = 0.3231$, $\mathcal{R}[\Phi(r_-)] = -\sqrt{2Z\Omega}$ does not occur, but $\mathcal{R}[\Phi(r_+)] = \sqrt{2Z\Omega}$ occurs at $r_+ = 0.7720$.

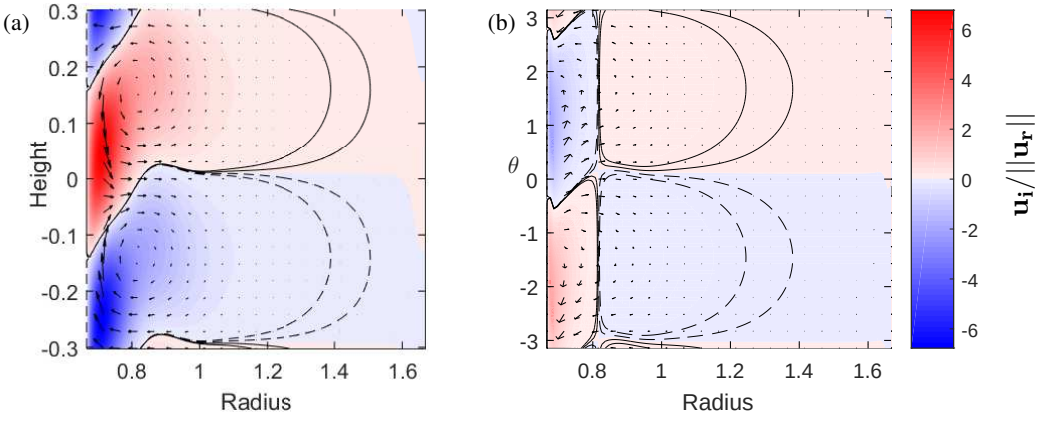

FIGURE S7. Type (i) plots (a), (b) as described in § 1.1. Example of the γ-mode, inner boundary-trapped SRI, as the critical viscous mode of instability for stratified Taylor-Couette flow. This is figure 7(a,b) of the main paper. The RI has actually morphed into an inner boundary-trapped mode, living on the inner boundary and steadily decaying outward. $\eta = 0.40$, $\mu = 0.45$, $m = 1$, $Fr = 1$, in region γ in figure 2, and this critical mode onsets at $Re = 6526.7$ with $k = 10.407$. $\omega = 0.7823$, $\mathcal{R}[\Phi(r_c)] = 0$ at $r_c = 0.816$, $\mathcal{R}[\Phi(r_-)] = -\sqrt{2Z\Omega}$ does not occur, and $\mathcal{R}[\Phi(r_+)] = \sqrt{2Z\Omega}$ does not occur either in the gap, $\max(|\Phi|) < N = 1$.

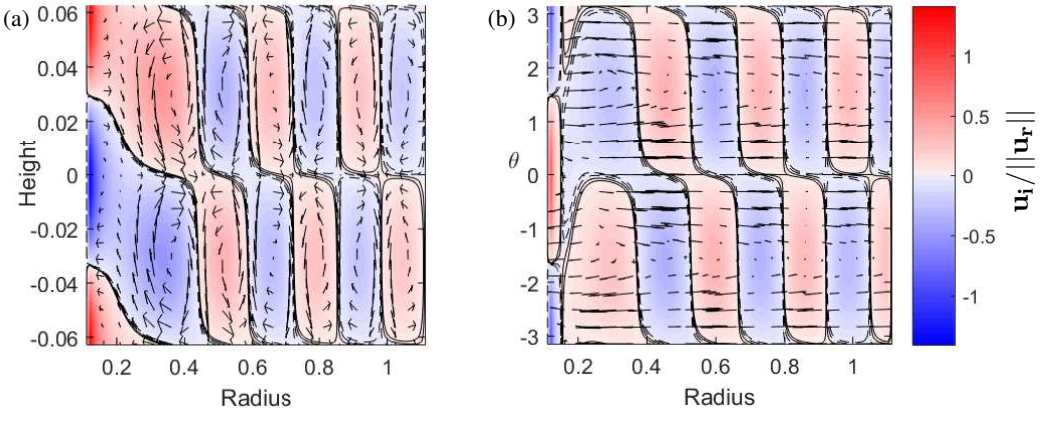

FIGURE S8. Type (i) plots (a), (b) as described in § 1.1. $\eta = 0.10$, $\mu = 0.10$, $m = 1$, $Fr = 1$, in region ζ in figure 2, and this mode, which is **not** the first to become unstable, onsets at $Re = 114199$ with $k = 50.126$. $\omega = 0.5803$. This mode has half a radial wavelength less between the gaps than figure S1, which is the critical mode at $\eta = \mu = 0.1$. $\mathcal{R}[\Phi(r_c)] = 0$ at $r_c = 0.1514$, $\mathcal{R}[\Phi(r_-)] = -\sqrt{2Z\Omega}$ does not occur, but $\mathcal{R}[\Phi(r_+)] = \sqrt{2Z\Omega}$ occurs at $r_+ = 0.2517$, $\max(|\Phi|) < N = 1$.

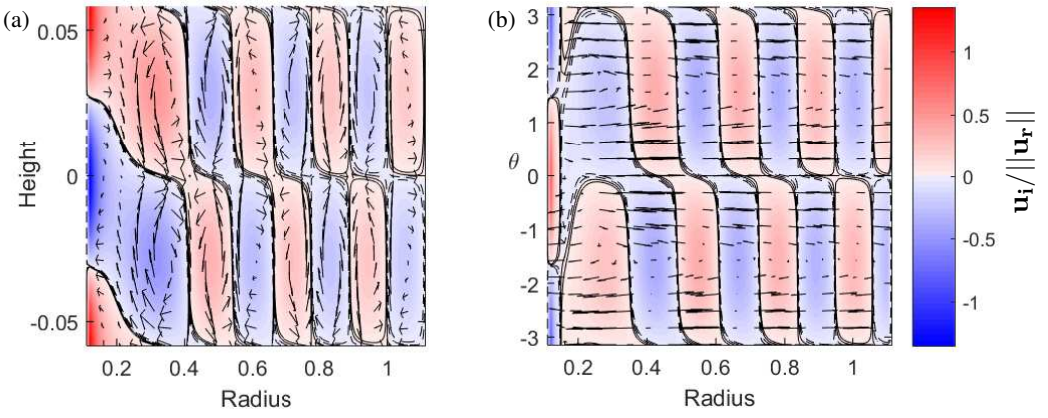

FIGURE S9. Type (i) plots (a), (b) as described in § 1.1. $\eta = 0.10$, $\mu = 0.10$, $m = 1$, $Fr = 1$, in region ζ in figure 2, and this mode, which is **not** the first to become unstable, onsets at $Re = 145040$ with $k = 54.06$. $\omega = 0.6016$. This mode has a very similar k to figure S1. As Re is increased above 12565.1, the growth rate initially increases and then starts to decrease. The mode restabilises as Re is further increased. If Re is increased yet further it goes unstable again at $Re = 145040$. The number of waves in the radial direction is similar to figure S1, though the shape of the eigenfunction is somewhat different. $\mathcal{R}[\Phi(r_c)] = 0$ at $r_c = 0.1482$, $\mathcal{R}[\Phi(r_-)] = -\sqrt{2Z\Omega}$ does not occur, but $\mathcal{R}[\Phi(r_+)] = \sqrt{2Z\Omega}$ occurs at $r_+ = 0.2426$, $\max(|\Phi|) < N = 1$.

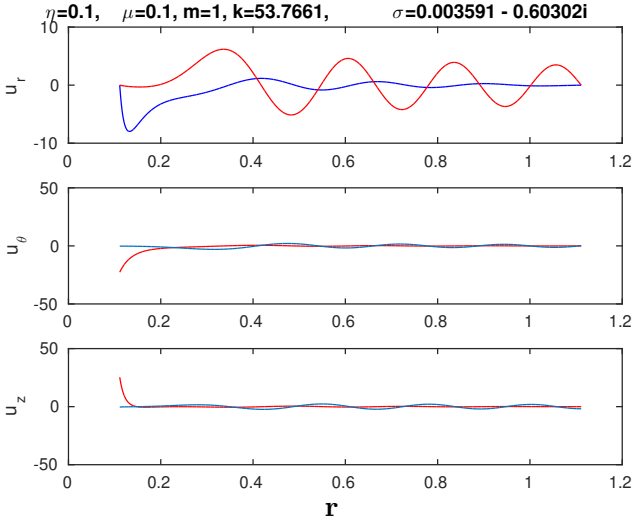

FIGURE S10. Type (iii) plot as described in § 1.3. Inviscid eigenfunctions at $\eta = 0.10$, $\mu = 0.10$, $m = 1$, $Fr = 1$, in region ζ in figure 2. Red is real part, blue is imaginary part. This local maximum of growth rate is attained at $k = 53.7661$, and the complex growth rate there is $0.003591 - 0.60302i$. Note the amplitudes of u_θ and u_z are large near the inner cylinder. The number of radial wavelengths in the inviscid plots is consistent with figures S1 and S9, which have similar k. This is the same case as figure S2 plotted in a different way with a different program to test our code. Eigenvalues are the same!

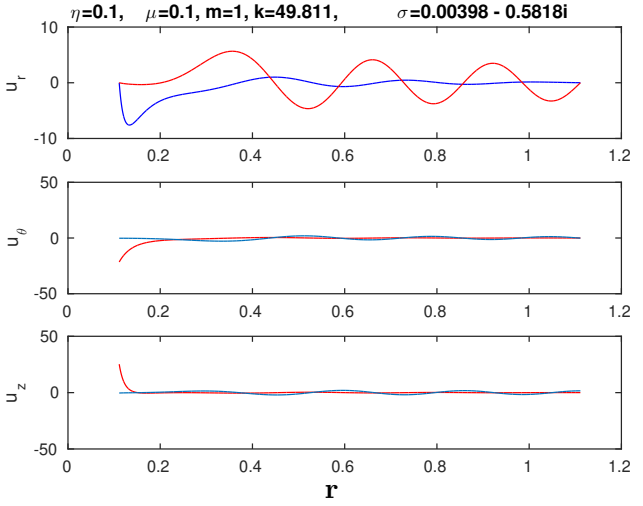

FIGURE S11. Type (iii) plot as described in § 1.3. Inviscid eigenfunctions at $\eta = 0.10$, $\mu = 0.10$, $m = 1$, $Fr = 1$, in region ζ in figure 2. Red is real part, blue is imaginary part. This local maximum of growth rate is attained at $k = 49.811$, and the complex growth rate there is $0.003982 - 0.5818i$. Note the amplitudes of u_θ and u_z are large near the inner cylinder. The number of radial wavelengths in these inviscid plots is half a wavelength less than those in figure S10.

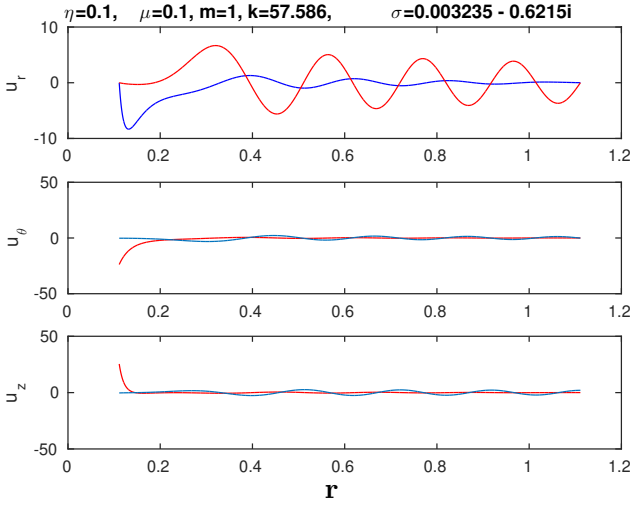

FIGURE S12. Type (iii) plot as described in § 1.3. Inviscid eigenfunctions at $\eta = 0.10$, $\mu = 0.10$, $m = 1$, $Fr = 1$, in region ζ in figure 2. Red is real part, blue is imaginary part. This local maximum of growth rate is attained at $k = 57.586$, and the complex growth rate there is $0.003235 - 0.6215i$. Note the amplitudes of u_θ and u_z are large near the inner cylinder. The number of radial wavelengths in these inviscid plots is half a wavelength more than those in figure S10.

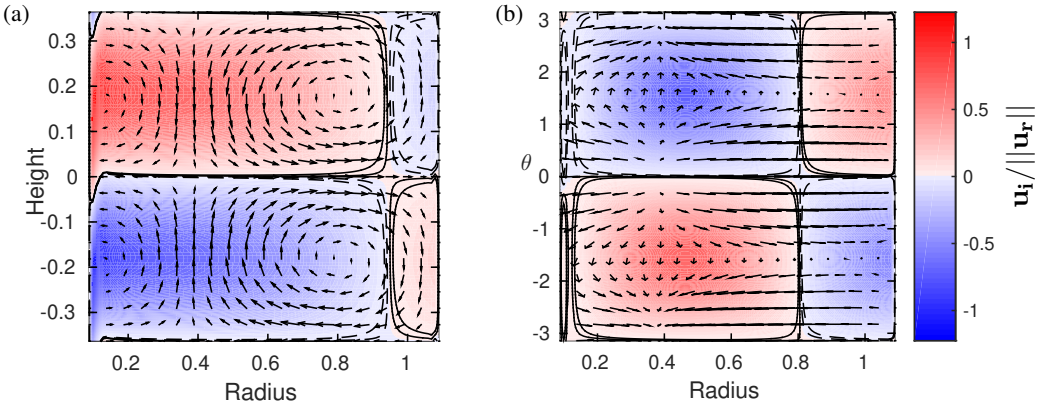

FIGURE S13. Type (i) plots (a), (b) as described in § 1.1. Wide-gap mode at the triple point T, shown in figure 2 of the main paper, which is dominant in region ε. $\eta = 0.081617$, $\mu = 0.057637$, $m = 1$, $Fr = 1$, with onset at $Re = 17493$ with $k = 8.644$, $\omega = 0.5834$. $\mathcal{R}[\Phi(r_c)] = 0$ at $r_c = 0.1510$, $\mathcal{R}[\Phi(r_-)] = -\sqrt{2Z\Omega}$ does not occur, but $\mathcal{R}[\Phi(r_+)] = \sqrt{2Z\Omega}$ occurs at $r_+ = 0.2503$.

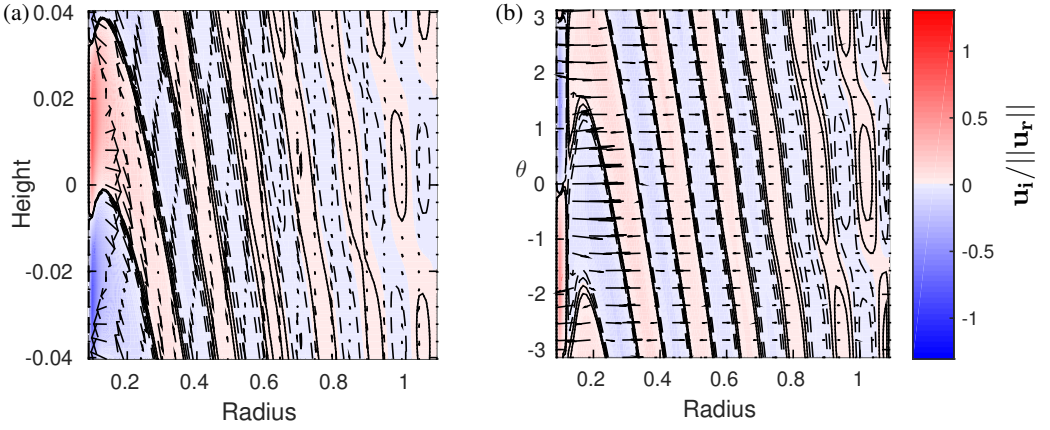

FIGURE S14. Type (i) plots (a), (b) as described in § 1.1. RI at the triple point T, as shown in figure 2 of the main paper, which is dominant in region ζ. $\eta = 0.081617$, $\mu = 0.057637$, $m = 1$, $Fr = 1$, with onset at $Re = 17493$ with $k = 77.93$, $\omega = 0.57124$. $\mathcal{R}[\Phi(r_c)] = 0$ at $r_c = 0.1529$, $\mathcal{R}[\Phi(r_-)] = -\sqrt{2Z\Omega}$ does not occur, but $\mathcal{R}[\Phi(r_+)] = \sqrt{2Z\Omega}$ occurs at $r_+ = 0.2559$.

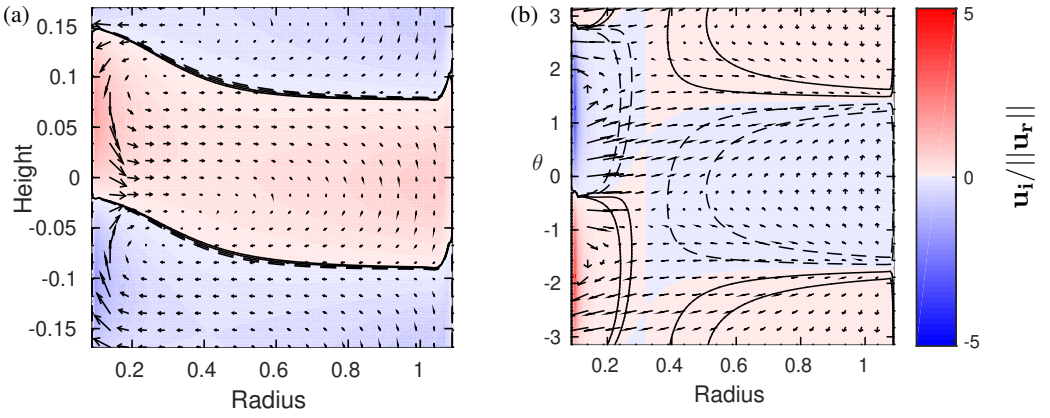

FIGURE S15. Type (i) plots (a), (b) as described in § 1.1. Inviscid-type mode at the triple point T, as shown in figure 2 of the main paper, which is dominant in region δ. $\eta = 0.081617$, $\mu = 0.057637$, $m = 1$, $Fr = 1$, with onset at $Re = 17493$ with $k = 18.65$. $\omega = 0.12436$. $\mathcal{R}[\Phi(r_c)] = 0$ at $r_c = 0.5792$, $\mathcal{R}[\Phi(r_-)] = -\sqrt{2Z\Omega}$ occurs at $r_- = 0.1506$, and $\mathcal{R}[\Phi(r_+)] = \sqrt{2Z\Omega}$ does not occur in the gap.

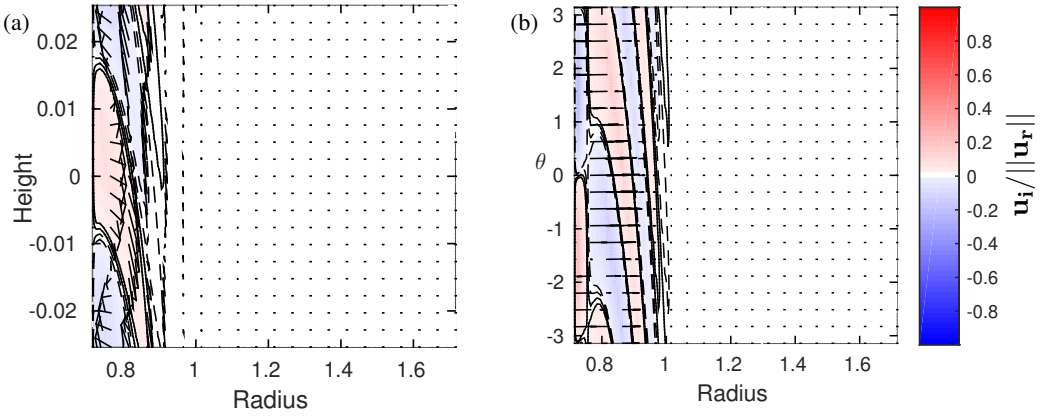

FIGURE S16. Type (i) plots (a), (b) as described in § 1.1. LeClerq et al. (2016) type mode: $\eta = 0.417$, $\mu = 0.17$, $m = 1$, $Fr = 2$ ($N = 0.5$). $Re = 10^6$ so this is not a neutrally stable mode but a growing mode. $\sigma = 0.06789 - 0.86135i$. $k = 123.9$ and this k maximises the growth rate at $Re = 10^6$ with these parameters. $\mathcal{R}[\Phi(r_c)] = 0$ at $r_c = 0.7704$. Because μ is below the Rayleigh critical value η^2, Z is negative and $(\mathcal{R}[\Phi(r_c)])^2 - 2Z\Omega$ is always positive, so it is always wave-like in the WKBJ-inviscid sense. $\mathcal{R}[\Phi(r)] = N$ at $r = 1.1850$ and there are no waves beyond this significant surface.

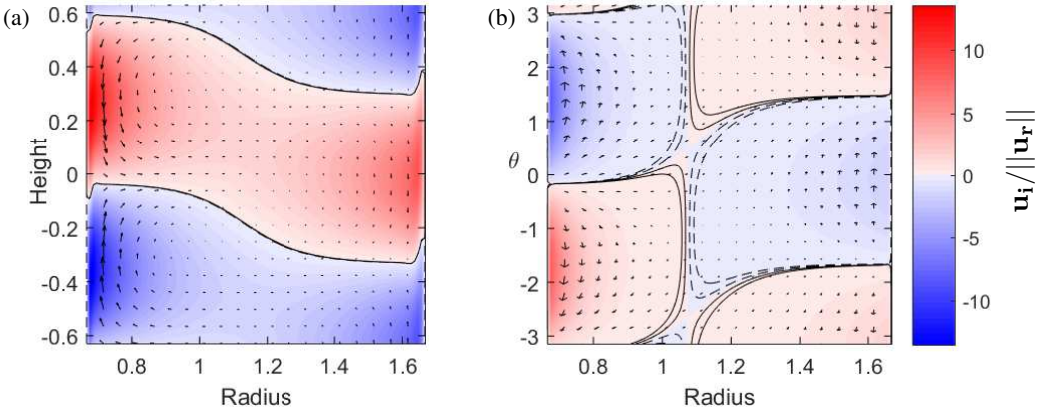

FIGURE S17. Type (i) plots (a), (b) as described in § 1.1. $\eta = 0.4$, $\mu = 0.45$, in region γ in figure 2. A Kelvin wave type viscous SRI at $Fr = 1$, $m = 1$ $Re = 71840$, $k = 5.00$, $\omega = 0.598$.
This is **not** the most unstable mode at these values of η, μ and Fr, which is figure 7 in the main paper, but it is at a local minimum of Re as k is varied: this can be seen by looking at figure 7(c) of the main paper. It is however the only clear Kelvin wave type instability we found at $Fr = 1$. $\mathcal{R}[\Phi(r_c)] = 0$ at $r_c = 1.0730$, $\mathcal{R}[\Phi(r_-)] = -\sqrt{2Z\Omega}$ doesn't occur, and $\mathcal{R}[\Phi(r_+)] = \sqrt{2Z\Omega}$ does not occur either in the gap.

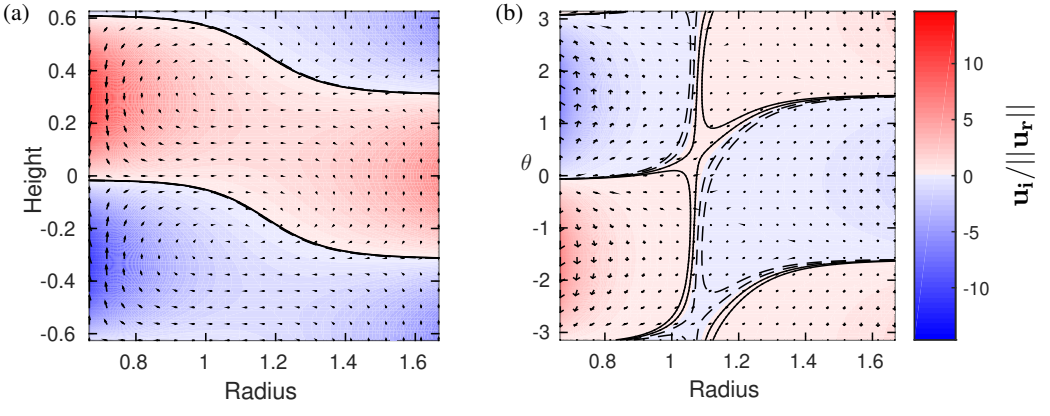

FIGURE S18. Type (ii) plots (a), (b) as described in § 1.1. $\eta = 0.4$, $\mu = 0.45$, $Fr = 1$, $m = 1$, in region γ in figure 2. Inviscid counterpart of the Kelvin wave type SRI, figure S17 above. Local maximum of growth rate over k at $k = 5.024$. Growth rate $\sigma = 0.003955$. Frequency $\omega = 0.59882$. Very similar to the viscous figure S17 above.

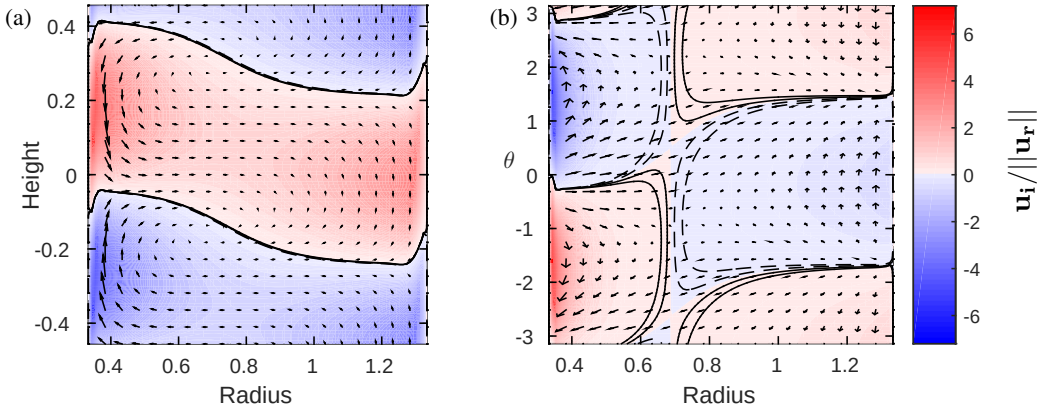

FIGURE S19. Type (i) plots (a), (b) as described in § 1.1. $\eta = 0.25$, $\mu = 0.25$, in region γ in figure 2 (but just above the γ-δ border). Viscous SRI with $Fr = 1, m = 1$ $Re = 13340$, $k = 6.89, \omega = 0.3883$. This is the inviscid-type mode which is **not** the most unstable mode at these parameters: since we are in region γ of figure 2 here, an inner boundary-trapped mode is the critical viscous mode here. This mode is intermediate between the Kelvin-wave-like figure S17 and the inviscid-type mode of figure S20 in region δ. There is less activity at the outer boundary than in figure S17, but more than in figure S20 below. $\mathcal{R}[\Phi(r_c)] = 0$ at $r_c = 0.6871$, $\mathcal{R}[\Phi(r_-)] = -\sqrt{2Z\Omega}$ doesn't occur, and $\mathcal{R}[\Phi(r_+)] = \sqrt{2Z\Omega}$ does not occur either in the gap.

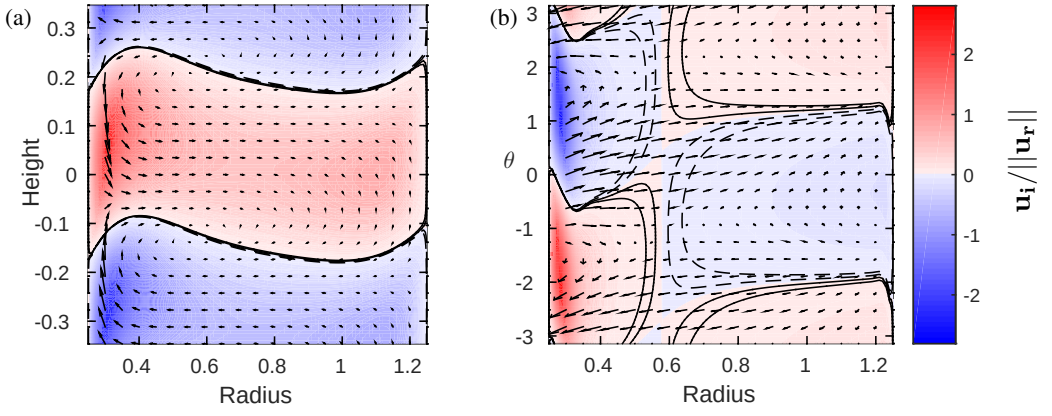

FIGURE S20. Type (i) plots (a), (b) as described in § 1.1. $\eta = 0.2$, $\mu = 0.1$, in region δ in figure 2, viscous SRI $Fr = 1$, $m = 1$ $Re = 670.1$, $k = 9.067$, $\omega = 0.2384$. $\mathcal{R}[\Phi(r_c)] = 0$ at $r_c = 0.577$, $\mathcal{R}[\Phi(r_-)] = -\sqrt{2Z\Omega}$ occurs at $r_- = 0.319$, and $\mathcal{R}[\Phi(r_+)] = \sqrt{2Z\Omega}$ does not occur in the gap.
This is figure 8(a,b) of the main paper in the alternative colour scheme. It is the inviscid-type mode example, region δ. Note that the Kelvin-wave-like mode of figure S17 has gradually morphed into this inviscid-type mode. All the viscous modes shown in figures S17, S19 and S20 have inviscid counterparts with a similar value of k.

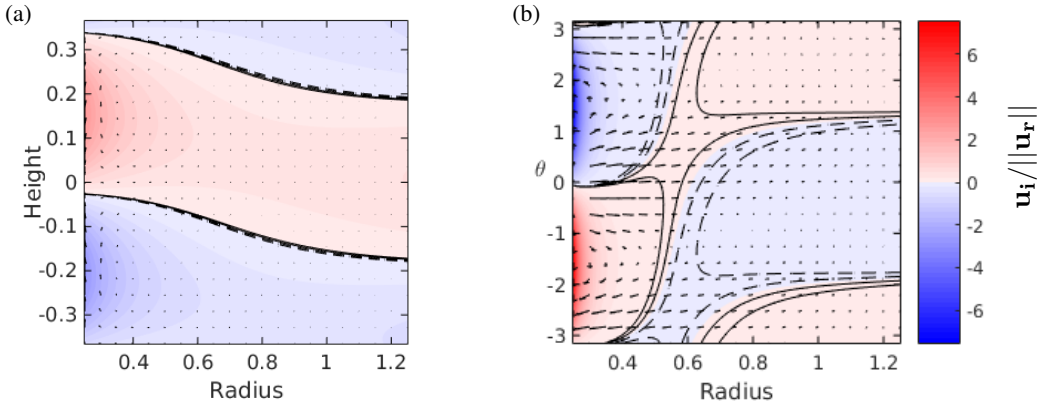

FIGURE S21. Type (ii) plots (a), (b) as described in § 1.1. $\eta = 0.2$, $\mu = 0.1$, $Fr = 1$, $m = 1$ in region δ in figure 2. Inviscid counterpart of figure S20 which is also figure 8(a,b), the example of the inviscid-type mode. Local maximum of growth rate over k at $k = 8.613$. Growth rate $\sigma = 0.02789$. Frequency $\omega = 0.24978$.

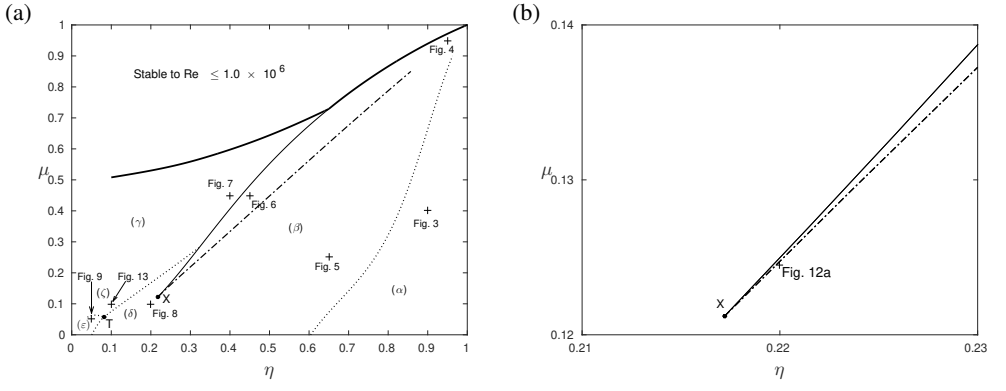

FIGURE S22. The left hand plot (a) is figure 2 of the main paper, but with a dot-dash curve coming out of point of continuity X added. This dot-dash curve is the curve on which the teardrop closed unstable domain becomes engulfed in the inviscid-type viscous mode above it. An explanation of how this can happen is given in § 7. An example of the teardrop configuration can be seen in figure 6 of the main paper, at $m = 1$ and k just above 4.

Just to the left of the dot-dash curve there is a closed unstable domain, but just to the right of the dot-dash curve there is just one unstable domain reaching to large values of Re.

The right hand plot (b) is an expanded version of figure 2, showing the neighbourhood of the point of continuity X. The cross marked Fig. 12a is at the point in the $\eta\mu$-plane corresponding to figure 12(a) in the main paper, just to the right of the dot-dash curve. Looking at figure 12(a) we see that the teardrop closed unstable domain has just been engulfed, consistent with the figure 12(a) value, $\eta = 0.22$, $\mu = 0.1245$, being just to the right of the dot-dash curve.